

Interface Engineering in Perovskite Solar Cells by Low Concentration of Phenylethyl Ammonium Iodide Solution in the Antisolvent Step

Teresa S. Ripolles,* Patricio Serafini, Carlos Redondo-Obispo, Esteban Climent-Pascual, Sofia Masi, Iván Mora-Seró,* and Carmen Coya*

In spite of the outstanding properties of metal halide perovskites, its polycrystalline nature induces a wide range of structural defects that results in charge losses that affect the final device performance and stability. Herein, a surface treatment is used to passivate interfacial vacancies and improve moisture tolerance. A functional organic molecule, phenylethyl ammonium iodide (PEAI) salt, is dissolved with the antisolvent step. The additive used at low concentration does not induce formation of low-dimensional perovskites species. Instead, the organic halide species passivate the surface of the perovskite and grain boundaries, which results in an effective passivation. For sake of generality, this facile solution-processed synthesis was studied for halide perovskite with different compositions, the standard perovskite MAPbI₃, and double cation perovskites, MA_{0.9}Cs_{0.1}PbI₃ and MA_{0.5}FA_{0.5}PbI₃, increasing the average photoconversion efficiency compared to the reference cell by 18%, 32%, and 4% respectively, observed for regular, n-i-p, and inverted, p-i-n, solar cell configurations. This analysis highlights the generality of this approach for halide perovskite materials in order to reduce nonradiative recombination as observed by impedance spectroscopy.

1. Introduction

Metal halide perovskite solar cells (PSCs) have attracted considerable attention due to their good light absorption, tunable bandgap, long charge diffusion lengths, and low manufacturing costs.^[1] To date, the highest power conversion efficiency (PCE) reported and certified has already exceeded 25.5%,^[2] being the most promising next-generation photovoltaic technologies in renewable energy. Interestingly, this outstanding performance has been reached with polycrystalline thin films less demanding, from the industrial point view,^[1b] than their crystalline counterparts. However, despite the benign defect physics of halide perovskites, the polycrystalline character of these materials leads to disorderly distribution of defects in the perovskite or at the grain boundaries, surfaces, and interfaces, that turns in losses

of on the power conversion efficiency (PCE) of PSCs.^[3] Therefore, advances in passivating-strategies are highly demanded and would ensure a viable commercial future for PSCs. Recently, significant attention has been paid to improve the stability of PSCs via passivation of grain-boundary and interface engineering.^[4]

To address this challenge, one of the most widely used passivating agents as additive is the organic halide salt phenylethyl ammonium iodide (PEAI).^[4,5] This iodide salt is composed by two components, a bulky organic chain with a benzene ring and an ammonium group (R-NH₃⁺) which represents PEA⁺. Added to perovskite precursors, the large PEA⁺ cation causes anionic layers in the 3D architecture to be isolated and transform into a 2D perovskite of general formula (RNH₃)₂A_{n-1}B_nX_{3n+1} (n = 1)^[6] or into a quasi-3D perovskite compositions.^[7] The improved phase stability of the corresponding films, due to less defects at the grain boundaries,^[8] efficiently increase the photovoltaic performance and the moisture stability of PSCs.^[8,9] In addition, PEA⁺ increases black phase stability,^[10] as in all-inorganic perovskite CsPbI₃, stabilizing the orthorhombic black phase (γ-CsPbI₃) under ambient condition and to avoid the yellow δ-CsPbI₃ formation, achieving high open circuit voltage over 1.3 V.^[11] Moreover, pure 2D (PEA)₂PbI₄ perovskite films prepared by blade-coating has an highly crystalline nature^[12]


T. S. Ripolles, C. Redondo-Obispo, C. Coya
Escuela Técnica Superior de Ingeniería de Telecomunicación
Universidad Rey Juan Carlos
28933 Madrid, Spain
E-mail: carmen.coya@urjc.es

T. S. Ripolles
Instituto de Ciencia de los Materiales de la Universidad de Valencia
46980 Paterna, Valencia, Spain
E-mail: teresa.ripolles@uv.es

P. Serafini, S. Masi, I. Mora-Seró
Institute of Advanced Materials (INAM)
Universitat Jaume I
12071 Castelló de la Plana, Spain
E-mail: sero@uji.es

C. Redondo-Obispo
Instituto de Ciencia de Materiales de Madrid
Consejo Superior de Investigaciones Científicas
28049 Madrid, Spain

E. Climent-Pascual
Escuela Técnica Superior de Ingenieros Industriales
Universidad Politécnica de Madrid
28006 Madrid, Spain

 The ORCID identification number(s) for the author(s) of this article can be found under <https://doi.org/10.1002/ente.202100890>.

DOI: 10.1002/ente.202100890

and pure 2D $(\text{PEA})_2\text{SnI}_4$ prepared by sequential vapor process of PEAI/SnI_2 shows less tendency to Sn oxidation.^[13]

Besides, the PEA^+ cation has hydrophobic nature, which improves the moisture resistance of interfaces perovskite/transporting layers. In this sense, PEA^+ cation is considered an excellent additive if it is added properly in the 3D halide perovskite thin film. In fact, the PEAI salt was deposited as buffer layer in the PSCs^[14] to control surface recombination. In particular, either on the top of the perovskite surface in order to retard the charge-carrier recombination process;^[5b,14b] or on the bottom of the perovskite layer to passivate defects of NiO_x and enhance the interface contact properties^[5a] were successfully employed in p-i-n configuration. In all cases, PEAI -modified PSCs show better moisture resistance and superior thermal stability. Regarding n-i-p structure, a thin film of PEAI salt was deposited between perovskite $\text{FA}_{1-x}\text{MA}_x\text{PbI}_3$ and spiro-OMeTAD, to decrease surface defects and nonradiative recombination of halide perovskite films for efficient PSCs.^[14a] The above-mentioned study demonstrated a high PCE of 23.34%. PEAI salt was also studied in carbon electrode-based PSCs without hole transport materials to improve the poor perovskite/carbon contact. Specially, PEAI was added in a post-treatment carbon electrode once the PSC was prepared and PEAI film was deposited between the perovskite/carbon as an ultrathin PEA_2PbI_4 layer.^[15] Due to the hydrophobic nature of carbon and 2D perovskite layers a large cell stability over 1000 h of exposure to ambient conditions was achieved.

However, this use of PEAI requires an additional fabrication step. Here, we propose to remove this further step by incorporating PEAI during the antisolvent step. The antisolvent additive engineering is another strategy to improve the perovskite structural properties and several additives have been used with success.^[16] However, PEAI has been less explored in these conditions.^[17] Bai et al. demonstrated a novel solution process to growth in situ a 2D layer together with 3D perovskite in order to suppress ion migration in the device and enhance the cell ambient stability. However, when 2D perovskite is synthesized, a balance between stability and efficiency is necessary due to the lower carrier mobility of 2D structure compared to 3D perovskites.^[18]

Herein, we delve into the study of the PEAI effects caused in several metal halide compositions when the organic iodide salt is dissolved in the antisolvent at low concentration (0.0002–0.012 M). The experimental method proposed here avoid an additional step to fabricate a bilayer perovskite/ PEAI composition which is typically used for this additive.^[5a–15] Instead, the PEAI is introduced in low concentrations. As far as we know, there is not references using this additive in such low amount, that it is an advantage in terms of material waste optimization. In order to study the generality of the approach, three different halide perovskite compositions, MAPbI_3 , $\text{MA}_{0.9}\text{Cs}_{0.1}\text{PbI}_3$, and $\text{MA}_{0.5}\text{FA}_{0.5}\text{PbI}_3$, and two different solar cell structures, regular n-i-p and inverted p-i-n configurations, were deeply investigated and characterized. These materials have been selected as the two formers are broadly studied and present a tetragonal structure and the later because it presents a cubic structure, again for sake of the generality of the analysis. It was found that the introduction of the PEAI salt in the perovskite during the antisolvent step has an impact on reducing the crystallite domain size for

all structures, as confirmed by X-ray diffraction (XRD), and stabilizes their optical absorption up to 1300 h in ambient conditions. The role of the additive in the solar cells induces an increase of the PCE in all cases, as results of the reduction of the charge recombination processes confirmed by impedance spectroscopy.

2. Results and Discussion

2.1. Perovskite Film

We exploit the antisolvent additive engineering approach^[16a] to introduce the PEAI salt at very low concentrations, 0.0002–0.012 M (see Experimental Section for more details), in three representative metal halide perovskites compositions, mainly standard MAPbI_3 , and double cation $\text{MA}_{0.9}\text{Cs}_{0.1}\text{PbI}_3$, and $\text{MA}_{0.5}\text{FA}_{0.5}\text{PbI}_3$. Henceforth, these perovskites are called MA , $\text{MA}_{0.9}\text{Cs}_{0.1}$, and $\text{MA}_{0.5}\text{FA}_{0.5}$, respectively.

Figure 1a–d shows the room temperature XRD profiles for the samples with different A-site compositions in the ABX_3 perovskite structure, with and without PEAI addition in the synthesis. The XRD data for all samples indicate that perovskite polycrystalline

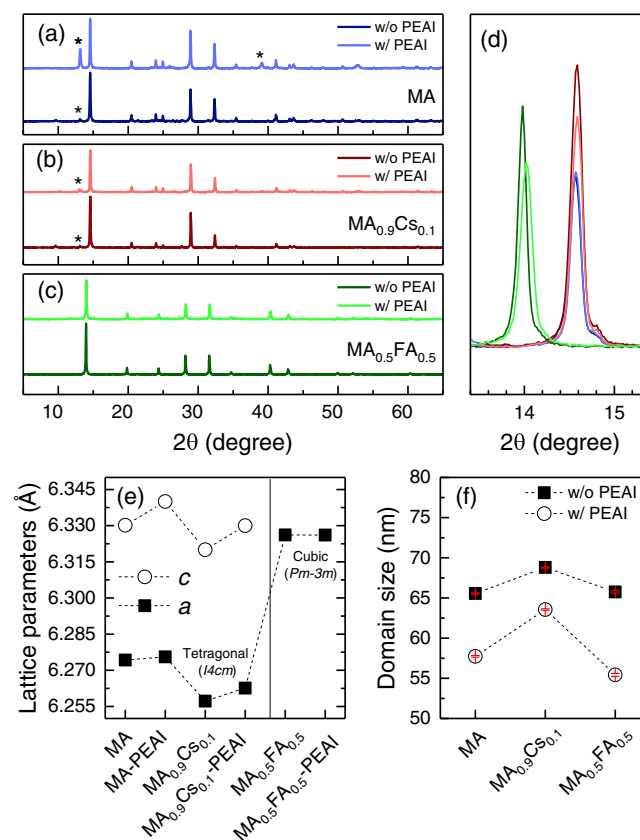


Figure 1. a–c) XRD profiles (Cu $K\alpha_1/\alpha_2$) of the MA, $\text{MA}_{0.9}\text{Cs}_{0.1}$, and $\text{MA}_{0.5}\text{FA}_{0.5}$ (with and without PEAI) films at 300 K. The asterisks indicate the impurity of PbI_2 . d) Zoom-in into the 13–16° 2θ range. e) Tetragonal $14cm$ (converted to pseudocubic) and cubic $Pm-3m$ lattice parameters. f) Variation of the average crystal domain size of samples with and without PEAI addition.

films were obtained for all compositions. The XRD profiles were indexed to an $I4cm$ tetragonal cell for MA and $MA_{0.9}Cs_{0.1}$ since the small MA cation gives rise to tetragonal structures with elongation in the c axis. But changing the small MA cation for the larger FA cation (case $MA_{0.5}FA_{0.5}$) increases the Goldschmidt tolerance factor (t) beyond the tetragonal limit ($t_{lim} = 0.972$),^[19] forming a cubic cell. In this case, $MA_{0.5}FA_{0.5}$ perovskite has been indexed to a $Pm-3m$ cubic cell. The halide perovskite lattice parameters were refined by a profile matching approach (see Figure S1, Supporting Information). For a better comparison of the obtained values, tetragonal parameters could be converted to pseudocubic parameters according to these equations: $a_{pc} = a_{tet}/\sqrt{2}$ and $c_{pc} = c_{tet}/2$. The lattice parameters as a function of the A-site composition could be seen in Figure 1e. In this figure, it can be seen how the presence of PEAI slightly increases the lattice parameters for the tetragonal compositions (MA and $MA_{0.9}Cs_{0.1}$), while it does not affect the cubic composition ($MA_{0.5}FA_{0.5}$).

The average crystal domain size has been obtained using the Williamson–Hall (WH) methodology (Figure S2, Supporting Information). The domain size as a function of the A-site composition in the films and the PEAI addition is shown in Figure 1f. PEAI reduces the crystallite size, likely indicative of more packed layers. When PEAI is not used, the domain size of MA and $MA_{0.5}FA_{0.5}$ is very similar (≈ 65.6 nm), while it slightly increases to 68.8 nm (5% increase) for the case of $MA_{0.9}Cs_{0.1}$. When PEAI is added, all domain sizes decrease, but the same trend is observed than without PEAI. To specify, there is a decrease of 11.9%, 7.6% and 15.8%, with final values of 57.7, 63.6, and 55.2 nm for MA, $MA_{0.9}Cs_{0.1}$, and $MA_{0.5}FA_{0.5}$, respectively.

The perovskite peak phase at 14.1° , which corresponds to the (110) reflection for MA and $MA_{0.9}Cs_{0.1}$ and to the (100) reflection for $MA_{0.5}FA_{0.5}$ have been followed over 1500 h by XRD of the perovskite layers under ambient conditions (see Figure S3, Supporting Information). Interestingly, perovskite phase hardly changes with time and remains almost constant with the presence of PEAI.

The top-view scanning electron microscopy (SEM) images were carried out (see Figure S4, Supporting Information). We found that the perovskite morphology was significantly altered by adding PEAI in the $MAPbI_3$ and $MA_{0.9}Cs_{0.1}PbI_3$ perovskites during the antisolvent, decreasing the grain size in both samples. At this point, it has to be noted that reducing the grain size is expected to be detrimental to efficiency due to recombination sites,^[20] as grain boundaries are the major recombination sites in iodide-based perovskites.^[21] However, other effects should be considered as the grain boundary passivation. The result of a trade-off between these two effects can cause that lower size grains produce high performance devices as we observed by the addition of PEAI into the antisolvent step. The phase purity of the synthesized perovskite samples of bare $MAPbI_3$ perovskite and $MAPbI_3$ with iodide salt PEAI were verified by proton nuclear magnetic resonance (1H NMR) spectroscopy. In order to have a net correspondence between the characterizations, we dissolved the prepared films in the proper deuterated solvent ($DMSO-d_6$). Due to this preparation method the samples were quite diluted (Figure S5a, Supporting Information) and the solvent peaks are predominant (dimethyl sulfoxide (DMSO) and residual water). In Figure S5b,c,

Supporting Information, it is clear the presence of the singlet corresponding to the ammonium group at 7.46 ppm and of the singlet from the aliphatic hydrogen of the MAI at 2.36 ppm, respectively,^[22] but there is no detectable trace of PEAI neither at high or low frequencies of the protonic spectra.^[23] Each characteristic peak mentioned above is independent of the PEAI addition. Therefore, both samples maintain similar chemical environments, thus indicating that the PEAI is not incorporated into the perovskite structure. Considering on the other hand, the effect in the morphology these studies point out to the grain boundaries for PEAI location.

In spite of the significant morphology changes induced by PEAI, in-plane DC dark resistivity (ρ) remains almost unaltered in the three compositions. The ρ -dependence with temperature in solar cells operation range temperature was measured for MA, $MA_{0.9}Cs_{0.1}$, and $MA_{0.5}FA_{0.5}$ thin films and is shown in Figure S6, Supporting Information. The resistivity for MA and $MA_{0.9}Cs_{0.1}$ compositions are slightly reduced and $MA_{0.5}FA_{0.5}$ perovskite remains unaltered with PEAI addition in the cubic regime. This reduction in ρ could be associated with an increase in the packing of the layer and an improvement in the grain interfaces that favours charge transport. ρ values at room temperature are 1.2×10^7 , 5.1×10^6 , and $0.4 \times 10^6 \Omega$ cm for pristine MA, $MA_{0.9}Cs_{0.1}$, and $MA_{0.5}FA_{0.5}$ perovskites, respectively, and, for perovskite thin films PEAI-doped are 2.4×10^6 , 3.6×10^6 , and $0.9 \times 10^6 \Omega$ cm, respectively, in accordance with previous works for $MAPbI_3$ polycrystalline samples.^[24]

The optical absorption spectra of bare perovskite and PEAI-doped perovskite samples are displayed in Figure S7, Supporting Information. The local minima of the second derivatives of the optical density (OD) spectra is useful to estimate the optical transition energies,^[25] which in this case, the first optical transition are located at 1.65 ± 0.04 eV for MA and $MA_{0.9}Cs_{0.1}$, and 1.59 ± 0.04 eV for $MA_{0.5}FA_{0.5}$, i.e., the optical bandgap E_g , corresponding to the described direct semiconductor type transitions at the R point in the pseudocubic Brillouin zone for perovskites.^[26] The full width at half-maximum of the second derivative is assumed as the error. PEAI addition does not modify the optical bandgap E_g , indicating that there are no changes in the stoichiometry of the synthesized thin films, in line with the NMR characterization. However, we found that the addition of PEAI has an important effect on the evolution of the absorption spectra under ambient conditions. In particular, the absorption coefficient remains constant up to 2.3 eV, which in concordance with the perovskite phase time evolution measured by XRD (Figure S3, Supporting Information, shows (110) peak evolution). Thus, it is confirmed that the PEAI salt stabilize the perovskite absorption in thin films over time, up to 1200 h, independently of the perovskite analyzed (Figure S8, Supporting Information), especially in the $MA_{0.5}FA_{0.5}$ thin films (Figure 2), possibly helped by the more packed morphology.

Normalized photoluminescence (PL) emission for MA, $MA_{0.9}Cs_{0.1}$ and $MA_{0.5}FA_{0.5}$ thin films is represented in Figure S7c, Supporting Information, and the maximum peak was located at 780, 770, and 807 nm, respectively, independently of the PEAI addition. These results are in line with the size of the cations introduced.^[27] In addition, PL confocal microscopy (Figure S9, Supporting Information) analyzed in an area of

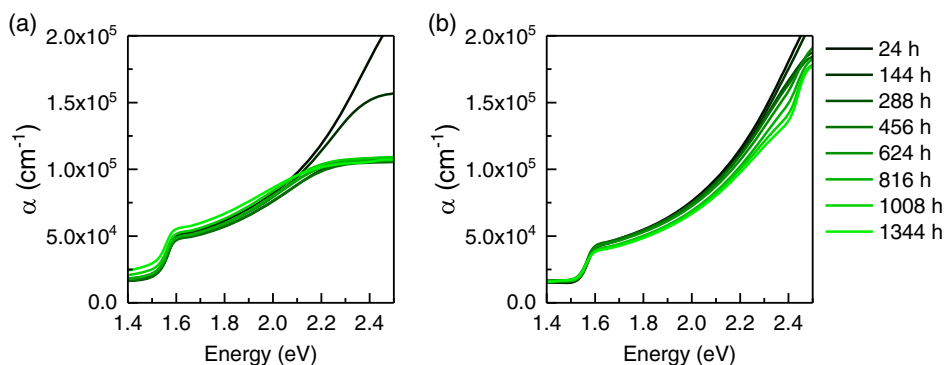


Figure 2. Absorption coefficient, α , over time of the $\text{MA}_{0.5}\text{FA}_{0.5}$ perovskite films, a) w/o and b) w/PEAI in the antisolvent solution.

$20 \times 20 \mu\text{m}^2$ reveals high uniformity in the emission observed in the PL mapping images (Figure S10, Supporting Information).

2.2. Perovskite Device

To study the influence of PEAI salt on the photovoltaic performance, two types of solar cells were fabricated (see Figure 3a), in regular and inverted architectures to further generalize the method. The analyzed architectures are, regular for MA and $\text{MA}_{0.9}\text{Cs}_{0.1}$ (ITO/ SnO_2 /MA or $\text{MA}_{0.9}\text{Cs}_{0.1}$ /spiro-OMeTAD/Au), and inverted for $\text{MA}_{0.5}\text{FA}_{0.5}$ (ITO/PEDOT:PSS/ $\text{MA}_{0.5}\text{FA}_{0.5}$ /PCBM/BCP/Al) (see Supporting Information for fabrication details).

For the optimal PSCs, the J - V characteristics under a simulated air mass (AM) of 1 sun illumination (100 mW cm^{-2}) are shown in Figure 3b, and the corresponding photovoltaic parameters are summarized in Table 1.

A positive significant impact is observed on the photovoltaic performance with PEAI salt addition in the antisolvent, independently of the active layer used, MA, $\text{MA}_{0.9}\text{Cs}_{0.1}$, and $\text{MA}_{0.5}\text{FA}_{0.5}$, and the architecture of the PSCs, either regular or inverted. Table 1 includes the statistical photovoltaic parameters of ten devices fabricated from different branches. It can be seen that these devices exhibit good reproducibility. In particular, $\text{MA}_{0.9}\text{Cs}_{0.1}$ -PEAI-based PSCs have a higher average efficiency among these PSCs, from 12.06% in pristine PSCs to 15.97% in $\text{MA}_{0.9}\text{Cs}_{0.1}$ -PEAI PSCs.

As we expected from the optical bandgap E_g , the $\text{MA}_{0.5}\text{FA}_{0.5}$ -based solar cells displayed lower open-circuit voltage, V_{oc} , close to 0.78 V, and an enhancement of V_{oc} for MA- and $\text{MA}_{0.9}\text{Cs}_{0.1}$ -based solar cells over 1 V, however, these values are also influence by the architecture and recombination processes. Interestingly, a V_{oc} increment is observed for all PEAI-based PSCs, which could be associated with a lower recombination rate,^[28] as pointed out later by impedance spectroscopy analysis. Same behavior was

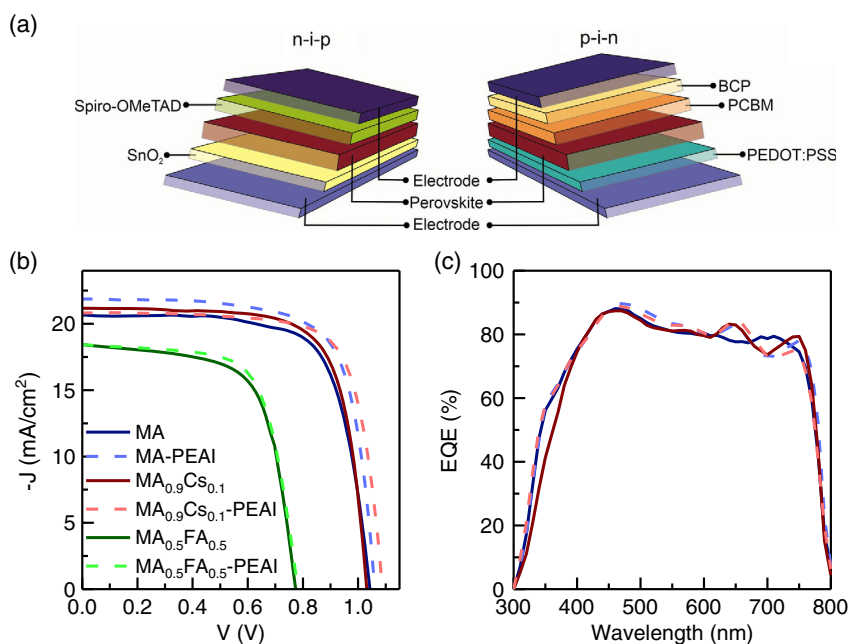


Figure 3. a) Device architectures n-i-p and p-i-n, b) photovoltage performance for champion devices under simulated 1 sun in forward sweep for the solar cells with (solid line) and without (dashed line) the salt PEAI effect, and c) EQE for the solar cells MA and $\text{MA}_{0.9}\text{Cs}_{0.1}$ perovskite compositions.

Table 1. Photovoltaic parameters of the p-i-n and n-i-p PSCs based on PEAI salt. It is included the champion solar cell and the average values with standard errors from ten devices fabricated in parallel.

Perovskite	Architecture	V_{oc} [V]	J_{sc} [mA cm^{-2}]	FF [%]	PCE [%]
MA	n-i-p	1.043 (1.02 ± 0.02)	20.685 (20.5 ± 0.6)	71.2 (62 ± 5)	15.35 (12.9 ± 1.4)
MA-PEAI	n-i-p	1.06 (1.07 ± 0.01)	21.86 (20.7 ± 1.0)	72.4 (69 ± 3)	16.77 (15.2 ± 1.2)
$\text{MA}_{0.9}\text{Cs}_{0.1}$	n-i-p	1.031 (1.01 ± 0.02)	21.143 (20.2 ± 0.6)	72.6 (59 ± 7)	15.83 (12.1 ± 2.0)
$\text{MA}_{0.9}\text{Cs}_{0.1}$ -PEAI	n-i-p	1.088 (1.07 ± 0.01)	20.83 (21.0 ± 0.5)	74.3 (71 ± 3)	16.84 (16.0 ± 1.0)
$\text{MA}_{0.5}\text{FA}_{0.5}$	p-i-n	0.773 (0.780 ± 0.006)	18.44 (16.3 ± 1.8)	66.10 (65.4 ± 2.0)	9.42 (8.3 ± 0.9)
$\text{MA}_{0.5}\text{FA}_{0.5}$ -PEAI	p-i-n	0.781 (0.780 ± 0.005)	18.42 (16.8 ± 1.3)	68.15 (66.5 ± 2.5)	9.80 (8.7 ± 0.8)

observed to short-circuit current, J_{sc} , and fill factor, FF, being the highest results for $\text{MA}_{0.9}\text{Cs}_{0.1}$ -based PSC to J_{sc} over 21 mA cm^{-2} and FF of 74.3%. Figure 3c presents the external quantum efficiency (EQE) spectrum of the regular PSCs. The photocurrent density was integrated from the spectrum (see Figure S11, Supporting Information), which reveals that the J_{sc} with a value of 20.23, 20.59, 20.19, and 20.38 mA cm^{-2} for PSCs of MA, MA-PEAI, $\text{MA}_{0.9}\text{Cs}_{0.1}$, $\text{MA}_{0.9}\text{Cs}_{0.1}$ -PEAI, respectively. J_{sc} obtained from the J - V measurement and the EQE spectrum are in good agreement, with a difference less than 5%.

As can be observed in Figure 3b, the PEAI treatment increases the performance of champion cells for all the analyzed materials and architectures, increasing PCE of PEAI-treated MA, $\text{MA}_{0.9}\text{Cs}_{0.1}$ and $\text{MA}_{0.5}\text{FA}_{0.5}$ champion cells respect reference by 9%, 6%, and 4%, respectively. Interestingly, for MA and $\text{MA}_{0.9}\text{Cs}_{0.1}$, the most efficient ones, average PCE is more significantly enhanced by 18% and 32%, respectively.

In order to further investigate the effect of PEAI treatment, impedance spectroscopy has been measured at open-circuit conditions with different light intensities for MA- and $\text{MA}_{0.9}\text{Cs}_{0.1}$ -based solar cells.^[29] The Nyquist plots at V_{oc} of impedance spectra at 1 sun are represented in Figure 4a. As it is conventionally observed in highly efficient PSCs, we observed mainly two different semicircles, at low-frequency (LF) and high-frequency (HF) ranges. In both devices measured it is observed a decrease

in width of the arc when PEAI is used which indicates a lower resistance or better transport due to the presence of the cation at grain boundary as mentioned before which will result in higher PCE. In order to analyze more careful these data, an equivalent circuit model previously reported has been used and it is represented in Figure 4b.^[30] In particular, the recombination resistance, R_{rec} , see Figure 4c, has been obtained by the fitting of impedance measurements, as the sum of the resistances of HF and LF arcs, considering transport-resistance negligible.^[30] It can be observed that independently of the halide perovskite layer, PEAI treatment increases recombination resistance, and consequently indicates a decrease of the nonradiative recombination rate. The process of recombination losses is reduced efficiently by PEAI addition, in concordance with the observed V_{oc} increment. The PEAI salt, despite the low concentrations, induces a grain boundary halide perovskite passivation and a reduction of interfacial recombination. Interestingly, the long-term stability is also slightly enhanced despite the low amount of additive, see Figure S12 and S13, Supporting Information.

3. Conclusions

In summary, we have demonstrated that adding PEAI salt at low concentration during the antisolvent step is one alternative to

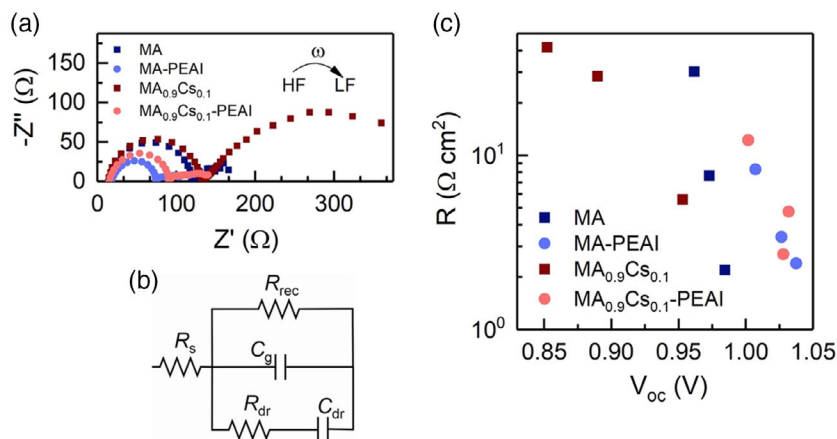


Figure 4. a) Nyquist plots at open-circuit voltage under 1 sun illumination intensity, b) equivalent circuit model composed of a series resistance, R_s , recombination resistance, R_{rec} , obtained as the sum of HF and LF arcs, considering the transport resistance negligible, which is in parallel to a HF capacitance, C_g , the geometrical capacitance, an in parallel with a RC branch (C_{dr} and R_{dr}), that splits the pattern in the HF and LF arcs,^[30] and c) recombination resistance at open circuit conditions for the PSCs w/o and w/PEAI in regular architecture.

improve PSCs' performance, without increasing the number of fabrication steps. The proposed method is tested in three representative compositions, the standard perovskite MAPbI₃, and double cation perovskites, MA_{0.9}Cs_{0.1}PbI₃ and MA_{0.5}FA_{0.5}PbI₃, and both, regular and inverted solar cells. PEAI reduces the crystallite domain size, enhancing the morphology. XRD and optical absorption confirms a stabilization effect of the perovskite phase in thin films for all compositions. For solar devices, the addition of PEAI leads to a PCEs increase, respect reference cells without treatment, by a very significant 18% and 32% for MA and MA_{0.9}Cs_{0.1}, respectively, and by a 4% for MA_{0.5}FA_{0.5}, and to a reduction of the recombination rate in all the cases. Besides, from NMR analysis, PEAI is not incorporated into the halide perovskite structure, reinforcing their passivating role at the grain boundaries, reducing traps states which results in the observed higher V_{oc} . Those findings found for a broad range of halide perovskite materials, with both tetragonal and cubic phase, and for both regular and inverted architectures, highlighting the generality of the simple approach. Decreasing the number of fabrication steps would have an important effect in the environmental impacts and cost of large-scale perovskite fabrication.

4. Experimental Section

Materials: All materials were reagent grade and were used as received. Perovskite precursors are lead iodide (PbI₂, >98%, from TCI and Aldrich) and methylammonium iodide (MAI, 98%, from Greatcellsolar and Dyesol). The solvents used are 2-propanol (99.7% from Carlo Erba), ethanol (96%) and acetone (99.25%) from PanReac, dimethyl formamide (DMF anhydrous 99.9%), DMSO (anhydrous 99.9%), chlorobenzene (CB anhydrous 99.8%), acetonitrile (MeCN anhydrous 99.8%), ethylacetate (EA anhydrous 99.8%), 4-tert-butylpyridine (TBP 96%), zinc powder (99.995%), and lithium bis(trifluoromethylsulfonyl)imide (Li-TFSI, 99.95%) from Sigma Aldrich. 2,20,7,70-tetrakis [N,N-di(4-methoxyphenyl)amino]-9,90-spirobifluorene (spiro-OMeTAD 99%) from Feiming chemical limited. The hydrochloric acid (HCl 37%) is from Aldrich. The electron transport layer such as SnO₂ colloid precursor is from Alfa Aesar (15% in H₂O colloidal dispersion) and PCBM is from Aldrich (>99.8%). The hole transport layer PEDOT:PSS Clevious P VP Al 4083 aqueous solution is from Heraeus. Indium tin oxide (ITO)-coated glass substrates (Pilkington TEC15, ≈15 Ω sq⁻¹).

Preparation of Perovskite Solutions: Three compositions have been synthesized, such as MAPbI₃, MA_{0.9}Cs_{0.1}PbI₃, and MA_{0.5}FA_{0.5}PbI₃. The solution preparation of each composition is as follow. Perovskite MAPbI₃ was prepared with a mixture of perovskite precursors of PbI₂ and MAI with a concentration of 1.4 M for each precursor and solved with a mixture of solvents, DMF:DMSO (4:1, v:v). Perovskite MA_{0.9}Cs_{0.1}PbI₃ follows the same trend than the perovskite standard MAPbI₃ and the precursor CsI is added with a concentration of 1.4 M and the precursors were solved with pure DMSO. The perovskite composition MA_{0.5}FA_{0.5}PbI₃ with a concentration of 0.65 M was prepared with a mixture of PbI₂, MAI, and FAI and dissolved with DMF:DMSO (4:1, v:v).

Device Fabrication n-i-p: Structure ITO/SnO₂/MAPbI₃ or MA_{0.9}Cs_{0.1}PbI₃/spiro-OMeTAD/Au. Glass substrates coated with ITO were etched by using zinc powder and pour over it drops of HCl 2 M. Then, glass was cleaned with deionized water, acetone, and ethanol in an ultrasonic cleaner for 15 min for each solvent one after the other. After being dried by air flow, the substrates were treated in an ultraviolet-ozone (UV-O₃) for 15 min to remove organic residues. Once the substrates were cleaned, the electron transport layer ETL SnO₂ was deposited in ambient at 25 °C and 30% RH by preparing a solution of SnO₂ 3% in water from the Alfa Aesar solution of 15%. The ETL was spin-coated onto the ITO substrates with a speed of 3000 rpm for 30 s, and then heated at 150 °C for 30 min. Once the SnO₂ film was prepared, the substrates were submitted to 20 min of UV-O₃ previously to perovskite deposition inside glovebox. A quantity of 50 μL

of perovskite was deposited over SnO₂ film by one-step spin coating at 4000 rpm for 20 s. At 8 s after starting the second step, an aliquot of 400 μL was added, either toluene or PEAI filtered solution with a concentration of 0.05 mg mL⁻¹. As soon as the spin coating was finished, the sample was moved to a hotplate at 130 °C for 10 min. After perovskite preparation, a 50 μL of hole transporting layer HTL (spiro-OMeTAD) solved in CB (85.5 mg mL⁻¹) doped with 28.8 μL of TBP and 17.8 μL of a stock solution of 520 mg mL⁻¹ of Li-TFSI in acetonitrile was spin-coated at 4000 rpm for 20 s onto the top annealed perovskite layers. Finally, Au electrode was deposited by thermal evaporation with a thickness of 80 nm.

Device Fabrication p-i-n: Structure ITO/PEDOT:PSS/MA_{0.5}FA_{0.5}PbI₃/PCBM/BCP/Al. Glass substrates patterned with ITO were treated in the same way than in the proceeding described previously. Once the substrates were completely cleaned, the next steps were carried out in the glovebox filled with nitrogen until end of the procedure. A diluted PEDOT:PSS solution (PEDOT:PSS:2-propanol, 5:1, v:v) were deposited by spin coater 4000 rpm for 45 s. Then, the HTL were heated at 130 °C for 30 min. The perovskite solution (150 μL) was dropped onto the PEDOT:PSS film and then spin coated at 1000 rpm for 10 s and then, at 6000 rpm for 30 s. As has been mentioned, the anti-solvent method used includes at 15 s of the second step add 450 μL either EA or PEAI filtered solution (0.05 mg mL⁻¹ solved with EA). The perovskite films were kept at room temperature for 30 min and then heated at 100 °C for 40 min. The ETL was formed by spin coating a solution of PCBM in CB (40 mg mL⁻¹) of 2000 rpm for 40 s and then, the film was treated at 60 °C for 10 min. On the top of the PCBM, a thin layer of BCP (5 mg mL⁻¹ in 2-propanol) was added by spin coater as 5000 rpm for 40 s. Finally, a thermal evaporation was carried out to evaporate Al.

Film Characterization—X-Ray Diffraction: The XRD diffractograms of the perovskite thin films were measured by Bruker D8 Advance diffractometer using Cu Kα radiation over a 2θ range between 5° and 65° with a step size of 0.02°.

Film Characterization—Optical Characterization: UV-vis absorption of the thin films was characterized using a UV-Vis-NIR spectrophotometer (Varian, Cary 5000) in the wavelength range of 300–900 nm.

Film Characterization—Steady-State Photoluminescence Emission: Confocal PL emission was measured with an inverted confocal microscope Leica TCS SP8 using an excitation wavelength of 561 nm with DPSS 561 laser employing a spectral resolution of 5 nm and 63 times of zoom image.

Film Characterization—Electrical Characterization: In-plane DC dark resistivity-temperature dependence was obtained from current-voltage characteristics with two-wire configuration due to the high resistance of the samples and a homemade Faradaic box. The dependences with increasing temperature have been measured in the 298–373 K range, with 10 K step size. The samples (thin films on glass substrate) were located on a hot plate with a K-type thermocouple right beside the sample to a process controller Electemp-TFT (Selecta). Current-voltage curves were measured at each temperature after 3 min stabilization, using a probe station and a Keithley 2450 Sourcemeter between two evaporated aluminum contacts.

Film Characterization—Scanning Electron Microscopy: SEM measurements were used to analyze the perovskite surface by employing a JEOL 7001 F microscope with an electron gun of 0.1–30 kV power which allow us to obtain an image at 20 000 times magnification.

Film Characterization—Hydrogen Nuclear Magnetic Resonance: NMR measurements were taken using a spectrometer Bruker Avance III HD 400 MHz employing solutions dissolved in DMSO-d₆ to analyze chemical shift between 0 and 10 ppm.

Device Characterization—Current-Voltage Measurement: J-V measurements were performed under AM 1.5 G (100 mW cm⁻²) conditions with a Wavelabs Sinus-70 AAA LED solar simulator with a Keithley 2450 sourcemeter. Each J-V curve was carried out from 0 to 1.15 V (forward direction) in a scan rate of 90 mV s⁻¹ without preconditioning. The spectrum of the solar simulator is monitored with reference intensity sensor in test plane in combination with fast feedback loop for automatic intensity correction and temperature control for the LEDs. The aging test was evaluated keeping the PSCs under dark and N₂ atmosphere.

Device Characterization—External Quantum Efficiency: EQE measurements were performed using a Xenon lamp with a monochromator Oriol Cornestone 130 which was used to measure along the wavelength of the spectrum. Prior measurement, calibration was done using a reference photodiode of silicon and each measurement was obtained using TRACQ BASIC software. Finally, EQE scans were taken from 300 to 810 nm every 10 nm.

Device Characterization—Impedance Spectroscopy: The IS was measured using a Potentiostat Autolab-PGSTAT204 in open circuit conditions. The light intensity was controlled by the Wavelabs Sinus-70 AAA LED solar simulator. For each light intensity, an AC 20 mV voltage perturbation was carried out and the frequency range was from 1 MHz to 100 mHz. Z-View software was used to fit the impedance spectra.

Supporting Information

Supporting Information is available from the Wiley Online Library or from the author.

Acknowledgements

T.S.R. acknowledges funding from Community of Madrid under the Talent fellowship 2017-T2/IND-5586 and project F660 financed by Community of Madrid and Rey Juan Carlos University. The authors acknowledge financial support by the Spanish Ministry of Science and Innovation under Projects PID2020-115514RB-I00, MAT2015-65356-C3-2-R, and PID2019-107314RB-I00. This work was partially supported by AYUDA PUENTE 2020 URJC. Associated Lab LABCADIO belonging to CM net laboratories ref 351 are also acknowledge. C.R.O. acknowledges funding from the Spanish Ministry of Science and Innovation under a FPI pre-doctoral contract (PRE2019-088433).

Conflict of Interest

The authors declare no conflict of interest.

Data Availability Statement

The data that support the findings of this study are available from the corresponding authors upon reasonable request.

Keywords

additives, halide perovskites, passivation, phenethylammonium iodide, solar cells

Received: October 6, 2021

Revised: November 3, 2021

Published online:

- [1] a) J. Y. Kim, J.-W. Lee, H. S. Jung, H. Shin, N.-G. Park, *Chem. Rev.* **2020**, *120*, 7867; b) R. Vidal, J.-A. Alberola-Borràs, N. Sánchez-Pantoja, I. Mora-Seró, *Adv. Energy Sustain. Res.* **2021**, *2*, 2000088.
- [2] M. Green, E. Dunlop, J. Hohl-Ebinger, M. Yoshita, N. Kopidakis, X. Hao, *Progr. Photovolt. Res. Appl.* **2021**, *29*, 3.
- [3] F. Gao, Y. Zhao, X. Zhang, J. You, *Adv. Energy Mater.* **2020**, *10*, 1902650.
- [4] a) Y. Gao, Y. Wu, Y. Liu, M. Lu, L. Yang, Y. Wang, W. W. Yu, X. Bai, Y. Zhang, Q. Dai, *Nanoscale Horiz.* **2020**, *5*, 1574; b) P. Guo, Q. Ye, X. Yang, J. Zhang, F. Xu, D. Shchukin, B. Wei, H. Wang, *J. Mater. Chem. A* **2019**, *7*, 2497.
- [5] a) Y. Liu, J. Duan, J. Zhang, S. Huang, W. Ou-Yang, Q. Bao, Z. Sun, X. Chen, *ACS Appl. Mater. Interfaces* **2020**, *12*, 771; b) F. Zhang, Q. Huang, J. Song, Y. Zhang, C. Ding, F. Liu, D. Liu, X. Li, H. Yasuda, K. Yoshida, J. Qu, S. Hayase, T. Toyoda, T. Minemoto, Q. Shen, *Sol. RRL* **2020**, *4*, 1900243.
- [6] J. Zhang, X. Zhu, M. Wang, B. Hu, *Nat. Commun.* **2020**, *11*, 2618.
- [7] C. Zuo, A. D. Scully, W. L. Tan, F. Zheng, K. P. Ghiggino, D. Vak, H. Weerasinghe, C. R. McNeill, D. Angmo, A. S. R. Chesman, M. Gao, *Commun. Mater.* **2020**, *1*, 33.
- [8] N. Li, Z. Zhu, C.-C. Chueh, H. Liu, B. Peng, A. Petrone, X. Li, L. Wang, A. K. Y. Jen, *Adv. Energy Mater.* **2017**, *7*, 1601307.
- [9] L. Zhou, Z. Lin, Z. Ning, T. Li, X. Guo, J. Ma, J. Su, C. Zhang, J. Zhang, S. Liu, J. Chang, Y. Hao, *Sol. RRL* **2019**, *3*, 1900293.
- [10] S. Masi, A. F. Gualdrón-Reyes, I. Mora-Seró, *ACS Energy Lett.* **2020**, *5*, 1974.
- [11] Q. Ye, F. Ma, Y. Zhao, S. Yu, Z. Chu, P. Gao, X. Zhang, J. You, *Small* **2020**, *16*, 2005246.
- [12] H. Duim, G. H. ten Brink, S. Adjokatse, R. de Kloe, B. J. Kooi, G. Portale, M. A. Loi, *Small Struct.* **2020**, *1*, 2000074.
- [13] W.-G. Choi, C.-G. Park, Y. Kim, T. Moon, *ACS Energy Lett.* **2020**, *5*, 3461.
- [14] a) Q. Jiang, Y. Zhao, X. Zhang, X. Yang, Y. Chen, Z. Chu, Q. Ye, X. Li, Z. Yin, J. You, *Nat. Photonics* **2019**, *13*, 460; b) B. Li, Y. Xiang, K. D. G. I. Jayawardena, D. Luo, Z. Wang, X. Yang, J. F. Watts, S. Hinder, M. T. Sajjad, T. Webb, H. Luo, I. Marko, H. Li, S. A. J. Thomson, R. Zhu, G. Shao, S. J. Sweeney, S. R. P. Silva, W. Zhang, *Nano Energy* **2020**, *78*, 105249.
- [15] K. Lee, J. Kim, H. Yu, J. W. Lee, C.-M. Yoon, S. K. Kim, J. Jang, *J. Mater. Chem. A* **2018**, *6*, 24560.
- [16] a) T. T. Ngo, I. Suarez, G. Antonicelli, D. Cortizo-Lacalle, J. P. Martinez-Pastor, A. Mateo-Alonso, I. Mora-Sero, *Adv. Mater.* **2017**, *29*, 1604056; b) Y.-J. Kang, S.-N. Kwon, S.-P. Cho, Y.-H. Seo, M.-J. Choi, S.-S. Kim, S.-I. Na, *ACS Energy Lett.* **2020**, *5*, 2535.
- [17] Y. Bai, S. Xiao, C. Hu, T. Zhang, X. Meng, H. Lin, Y. Yang, S. Yang, *Adv. Energy Mater.* **2017**, *7*, 1701038.
- [18] S. Zhang, S. M. Hosseini, R. Gunder, A. Petsiuk, P. Caprioglio, C. M. Wolff, S. Shoaee, P. Meredith, S. Schorr, T. Unold, P. L. Burn, D. Neher, M. Stolterfoht, *Adv. Mater.* **2019**, *31*, 1901090.
- [19] W. Li, M. U. Rothmann, Y. Zhu, W. Chen, C. Yang, Y. Yuan, Y. Y. Choo, X. Wen, Y.-B. Cheng, U. Bach, J. Etheridge, *Nat. Energy* **2021**, *6*, 624.
- [20] H. D. Kim, H. Ohkita, H. Benten, S. Ito, *Adv. Mater.* **2016**, *28*, 917.
- [21] R. Long, J. Liu, O. V. Prezhdo, *J. Am. Chem. Soc.* **2016**, *138*, 3884.
- [22] S. Masi, F. Aiello, A. Listorti, F. Balzano, D. Altamura, C. Giannini, R. Calciandro, G. Uccello-Barretta, A. Rizzo, S. Colella, *Chem. Sci.* **2018**, *9*, 3200.
- [23] G. Min, Y. Yun, H.-J. Choi, S. Lee, J. Joo, *J. Industr. Eng. Chem.* **2020**, *89*, 375.
- [24] a) C. C. Stoumpos, C. D. Malliakas, M. G. Kanatzidis, *Inorg. Chem.* **2013**, *52*, 9019; b) A. Pisoni, J. Jačimović, O. S. Barišić, M. Spina, R. Gaál, L. Forró, E. Horváth, *J. Phys. Chem. Lett.* **2014**, *5*, 2488.
- [25] a) C. Coya, C. Ruiz, Á. L. Álvarez, S. Álvarez-García, E. M. García-Frutos, B. Gómez-Lor, A. de Andrés, *Org. Electron.* **2012**, *13*, 2138; b) J. Bartolomé, E. Climent-Pascual, C. Redondo-Obispo, C. Zaldo, Á. L. Álvarez, A. de Andrés, C. Coya, *Chem. Mater.* **2019**, *31*, 3662.
- [26] a) M. Shirayama, H. Kadowaki, T. Miyadera, T. Sugita, M. Tamakoshi, M. Kato, T. Fujiseki, D. Murata, S. Hara, T. N. Murakami, S. Fujimoto, M. Chikamatsu, H. Fujiwara, *Phys. Rev. Appl.* **2016**, *5*, 014012; b) A. M. A. Leguy, P. Azarhoosh, M. I. Alonso, M. Campoy-Quiles,

- O. J. Weber, J. Yao, D. Bryant, M. T. Weller, J. Nelson, A. Walsh, M. van Schilfgaarde, P. R. F. Barnes, *Nanoscale* **2016**, *8*, 6317.
- [27] a) Y. Zhang, G. Grancini, Y. Feng, A. M. Asiri, M. K. Nazeeruddin, *ACS Energy Lett.* **2017**, *2*, 802; b) Y. Chang, L. Wang, J. Zhang, Z. Zhou, C. Li, B. Chen, L. Etgar, G. Cui, S. Pang, *J. Mater. Chem. A* **2017**, *5*, 4803.
- [28] W. Tress, N. Marinova, O. Inganäs, M. K. Nazeeruddin, S. M. Zakeeruddin, M. Graetzel, *Adv. Energy Mater.* **2015**, *5*, 1400812.
- [29] D. Pitarch-Tena, T. T. Ngo, M. Vallés-Pelarda, T. Pauporté, I. Mora-Seró, *ACS Energy Lett.* **2018**, *3*, 1044.
- [30] S.-M. Yoo, S. J. Yoon, J. A. Anta, H. J. Lee, P. P. Boix, I. Mora-Seró, *Joule* **2019**, *3*, 2535.